Site-selective characterisation of electron trapping centres in relation to chemistry, structural state and mineral phases present in single crystal alkali feldspars

RIEDESEL, S <http://orcid.org/0000-0003-2936-8776>, KUMAR, R <http://orcid.org/0000-0001-7658-459X>, DULLER, GAT <http://orcid.org/0000-0002-2694-4590>, ROBERTS, HM <http://orcid.org/0000-0001-9649-2377>, BELL, AMT <http://orcid.org/0000-0001-5038-5621> and JAIN, M <http://orcid.org/0000-0002-8942-7566>

Site-selective characterisation of electron trapping centres in relation to chemistry, structural state and mineral phases present in single crystal alkali feldspars

Riedesel, S.[1,2], Kumar, R.[3,4], Duller, G.A.T.[1], Roberts, H.M.[1], Bell, A.M.T.[5], Jain, M.[4]

[1] Department of Geography and Earth Sciences, Aberystwyth University, United Kingdom
[2] Cologne Luminescence Laboratory, Institute of Geography, University of Cologne, Germany
[3] RLAHA luminescence dating laboratory, Oxford University, United Kingdom
[4] Department of Physics, Technical University of Denmark, DTU Risø Campus, Denmark
[5] Materials and Research Engineering Institute, Sheffield Hallam University, United Kingdom

Keywords

Feldspar, trap depth, IRPL, radioluminescence, photoluminescence, spectroscopy

Abstract

Feldspars are ubiquitous natural dosimeters widely used in luminescence dating. Despite decades of research, the lattice defects as well as the mechanisms involved in luminescence production in feldspars remain poorly understood. The recently developed method of infrared-photoluminescence (IRPL) excitation-emission spectroscopy has revealed the presence of two electron trapping centres emitting IRPL at 1.3 eV and 1.41 eV ($IRPL_{1.3}$ and $IRPL_{1.41}$ centres), and it enables detailed investigations into the ground and excited state energies of these centres.

Here we make measurements of a range of single crystal alkali feldspars to understand the effects of feldspar chemical composition, crystal structure and framework disorder on the physical characteristics of $IRPL_{1.3}$ and $IRPL_{1.41}$ electron trapping centres. Measurements of our sample suite reveals IRPL and IR-RL emissions at 1.41 eV, 1.3 eV and, for the first time, at 1.2 eV. Our results show that whilst the $IRPL_{1.3}$ trapping centre is unaffected by the M site cation occupancy, the presence of $IRPL_{1.41}$ trapping centres seems to be linked to the presence of K^+ ions on M sites. However, no clear trends in IRPL and IR-RL emission energies and signal intensities with chemical composition of the

samples were found. Exploring the effect of framework disorder on $IRPL_{1.3}$ and $IRPL_{1.41}$ emissions revealed no significant changes to IRPL and IR-RL emission energies or ground state energies of the trapping centres, suggesting that the corresponding defects are not located on bridging O ions. Variations in ground state energies across the whole sample suite range from 2.04 eV to 2.20 eV for the $IRPL_{1.3}$ centre and from 2.16 eV to 2.46 eV for the $IRPL_{1.41}$ centre. Variations in trap depth seem to be driven by other factors than sample chemistry, degree of Al^{3+} disorder and number of phases present in a single crystal feldspar. Interestingly, the IR resonance peak is invariant between samples.

Regarding the use of IRPL in luminescence dating, we show that optical resetting differs for the three different emissions, with the emission at ~1.41 eV not being reset in some samples even after 18 hours of solar bleaching.

1 Introduction

Due to their ability to store charge within defects in the crystal lattice, feldspar minerals are widely used as natural luminescence dosimeters (e.g. Huntley et al., 1985; Hütt et al., 1988). Despite their routine and widespread use, the crystal defects and the physical processes involved in luminescence production in feldspars are not yet fully understood. In particular, the crystal defects responsible for the electron trapping centres in feldspars remain unknown, and the observed variations in luminescence across samples, or across single grains extracted from the same samples remain poorly understood.

By comparing photoluminescence (PL) and radioluminescence (RL) emissions of a lead-rich K-feldspar (amazonite) with those of a lead-doped potassium chloride, Erfurt (2003) suggested that the electron trap in feldspars is associated with Pb^{2+} ions substituting for K^{+} ions in the lattice of K-feldspars. Based on observing polarization effects during optical transitions in a sample of

orthoclase, Short (2004) inferred the electron trap in that sample to be located at a tetrahedral site on the framework. More recently, based on infrared photoluminescence (IRPL), Kumar et al. (2018, 2020a) proposed that the defect acting as an electron trapping centre is located in two different lattice environments within the feldspar lattice resulting in two different types of trapping centres (referred to as the $IRPL_{1.41}$ and $IRPL_{1.3}$ centre, where the subscript denotes the emission energy in eV). The observations by Erfurt (2003) and Short (2004) are only based on single alkali feldspar samples and the samples used by Kumar et al. (2018, 2020a) were primarily feldspars separated from sediments which therefore inevitably consisted of grains with a range of chemical compositions. Kumar et al. (2020a) also presented results for two single crystal specimens; one of these samples is a microcline perthite (K8; Baril, 2004) and for the other sample (R28) only the chemical composition is available (95 % K-feldspar, cf. Poolton et al. 1995). Kumar et al. (2020a) found that the electron trap depth varied from sample to sample and between the two measured IRPL emissions, with a minimum trap depth of 1.90 eV ($IRPL_{1.3}$ centre) and a maximum trap depth of 2.38 eV ($IRPL_{1.41}$ centre).

Since feldspars are complex framework silicates, properties inherent to the sample's crystal structure, in addition to the chemistry, could influence electron trapping centres in feldspars. Despite previous efforts, it remains to be established whether (i) electron traps in feldspars are associated with K^+ ions (Erfurt, 2003), (ii) if they occupy tetrahedral sites (Short, 2004), (iii) whether the same crystal defect which captures electrons in the feldspar crystal lattice is indeed located in two different crystallographic environments resulting in two different trapping centres (Kumar et al., 2018, 2020a) or (iv) if neither of these suggestions holds true and further possibilities need to be considered.

Recently, Kumar et al. (2020a) described an approach for constraining electron trap ground and excited state energies using low temperature infrared-photoluminescence (IRPL) excitation-emission spectroscopy. In this paper we apply this technique to a range of chemically and structurally

different single crystal feldspars in order to investigate the questions mentioned above. We have purposefully chosen single crystal feldspars to avoid any averaging of the measured luminescence arising due to a variety of grains present within a sediment sample. The samples used in the present study have previously been explored by Riedesel et al. (2021), who investigated changes in the recombination centres due to variations in samples chemistry, structural state (distribution of Al^{3+} ions on T sites) and number of phases present within a single crystal (i.e. single phase feldspars and perthites). By measuring thermoluminescence (TL) emission spectra and infrared stimulated luminescence (IRSL) fading rates, Riedesel et al. (2021) found that the structural state and the presence of perthite interfaces influence the blue luminescence emission and its fading rate. In the present article, we aim to see whether the chemical and mineralogical properties inherent to the same samples influence the presence as well as the properties of electron trapping centres in feldspars. In particular we explore the following questions: Are electron trapping centres, their ground and excited state energies, as well as RL and PL emissions related to (re)trapping of electrons in these centres, influenced by (1) the K- or Na-content of the samples, (2) the number of mineral phases present within a single crystal (i.e. whether it is single phase or perthitic), and/or (3) disorder of Al^{3+} ions on the Si,Al-framework? Answers to these questions will lead us closer to identifying which type(s) of defect(s) function(s) as electron trapping centres in feldspars.

2 Brief overview of the structure and chemistry of feldspars

Feldspars are complex framework silicates, consisting of $(Si,Al)O_4$ tetrahedra, which build the framework of the feldspar crystal lattice. Within the framework there are four tetrahedral positions occupied by Si^{4+} or Al^{3+} ions. The framework has a net negative charge, which is offset by large cations, predominantly Na^+, K^+ and Ca^{2+}. These cations occupy cavities in the framework termed M sites (Deer et al., 2013, p. 248). The compositional variability of most feldspars is accommodated by three end members, each with a different M site cation: $KAlSi_3O_8$ (K-feldspar), $NaAlSi_3O_8$ (Na-feldspar) and $CaAl_2Si_2O_8$ (Ca-feldspar). The solid solution between K- and Na-feldspar is termed the

alkali feldspar series and the solid solution between Na- and Ca-feldspar is referred to as plagioclases. In this paper we focus on the alkali feldspar solid solution series and its end members. In alkali feldspars the ratio of Si^{4+} and Al^{3+} on the framework is 3:1, and the degree of disorder of the tetrahedral site occupancy by these ions dictates the structural state of alkali feldspars. In the high-temperature K-feldspar (monoclinic high sanidine), Al^{3+} has an equal (25 %) chance of occupying any of the four tetrahedral sites ($T_1(0)$, $T_1(m)$, $T_2(0)$ and $T_2(m)$) within the more open alkali feldspar framework. During slow cooling, as the framework contracts, Al^{3+} diffuses into either of the two T_1 sites (giving the monoclinic low sanidine, also referred to as orthoclase). With continued slow-cooling, Al^{3+} preferentially diffuses into one of the two T_1 sites ($T_1(0)$), causing a change in symmetry from monoclinic (sanidine, with the greatest disorder) to triclinic (ordered K-feldspar maximum microcline, e.g. Stewart and Ribbe, 1969; Deer et al., 2013, p. 256-257). Another impact of cooling of feldspar is exsolution. Whilst at high temperature (> 1000 °C) a solid solution between the alkali feldspar end members exists, cooling of magma and of metamorphic rocks results in unmixing of K- and Na-rich phases in the alkali feldspars. Alkali feldspars with exsolution features, where K- and Na-rich phases form intergrowths, are termed perthites.

Variations in sample chemistry, exsolution and the degree and range of disorder of Al^{3+} on the framework might influence the luminescence of feldspars. It has been shown that impurity ions (e.g. Fe^{3+} or Mn^{2+}) can function as luminescence centres in feldspars (e.g. Telfer and Walker, 1978) and that the degree of framework disorder influences the blue luminescence emission intensity and its stability (Finch and Klein, 1999; Riedesel et al., 2021). Suggestions have been made regarding potential electron traps in feldspars (Speit and Lehmann, 1982a) and their locations (Erfurt, 2003; Short, 2004), however more work is needed to successfully link electron trapping centres to physical defects or structural variations in the feldspar crystal lattice.

3 Materials and Methods

3.1 Samples

The suite of eight feldspar samples used in this study consists of single crystal feldspar specimens of the alkali feldspar solid solution series and their end members, microcline and albite. The samples were previously investigated by Riedesel et al. (2021) who explored variability in TL emission spectra and IRSL fading rates with mineralogical properties of the samples. The chemistry of the samples was constrained using X-ray fluorescence (XRF), and semi-quantitative phase analyses were achieved using X-ray diffraction (XRD). Details regarding XRD and XRF measurement conditions and results can be found in Riedesel et al. (2021).

The samples include a range of alkali feldspar varieties including end members (Fig. 1). Sample FSM-13 is a single-phase microcline (98.5 % K-feldspar) and CLBR a single-phase albite specimen (99.3 % Na-feldspar). FSM-3 (82.5 % K-feldspar), FSM-14 (78.3 % K-feldspar) and FSM-5 (74.8 % K-feldspar) are perthites, as identified by XRD and optical examination using an optical microscope. These perthites are comprised of microcline and albite. FSM-6 (74.4 % K-feldspar) is a perthite, which consists of orthoclase and albite. FSM-3, FSM-6 and FSM-14 are cryptoperthites. FSM-5 is a macroperthite.

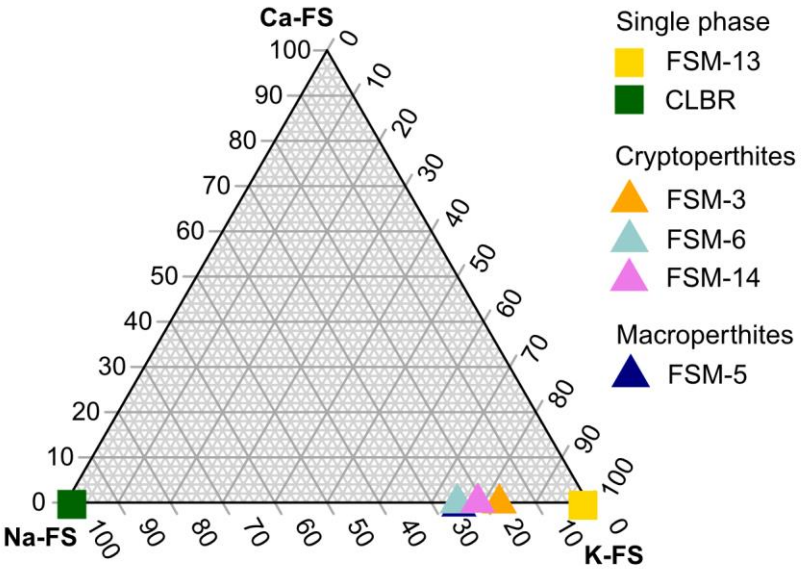

Fig. 1. Feldspar composition of the samples. The relative compositions of K-, Na- and Ca-feldspar were calculated using stoichiometric conversion of the XRF results.

Whilst these samples allow a comparison of excitation and emission spectra in regard to sample chemistry and the number of phases present (i.e. single phase or perthitic), two samples (FSM-6 and FSM-13) were selected for a heating experiment with the aim to artificially disorder the tetrahedral site occupancy by Al^{3+} ions. Details regarding this experiment are given in Riedesel et al. (2021). The success of the heating experiment was checked by analysing X-ray diffraction peak shape and position and this revealed that samples FSM-6 and FSM-13 were successfully disordered during the experiment (Riedesel et al., 2021). The samples are designated FSM-6LH and FSM-13LH after the heating experiment.

3.2 Radioluminescence and photoluminescence emission spectra

Radioluminescence (RL) and photoluminescence (PL) emission spectra were measured using the Risø station for CryOgenic Luminescence Research (COLUR) at DTU Physics, Technical University of Denmark. Prior to any luminescence measurements, the samples were bleached for 18 hours in a Hönle SOL2 solar simulator. Afterwards the sample was mounted as grains or shards (max. 1 mm diameter) on a Cu sample holder using carbon tape. The sample holder of COLUR is attached to a closed-loop He-cryostat, allowing measurements to be performed between 7 and 300 K. All RL and PL emission spectra presented in this paper were measured at 7 K. We chose the lowest possible measurement temperature in our measurement system of 7 K to minimise any spectral broadening arising from lattice vibrations. This allowed us to obtain the highest possible peak resolution required for our investigations. One sub-sample was measured per sample.

RL emission spectra were measured during irradiation using a filament-based X-ray tube with a Cu anode, operated at 40 kV anode voltage and 100 µA anode current, delivering ~0.06 Gy/s at the sample position. PL emission spectra were measured before and between irradiation steps. RL and PL emission spectra were recorded in the wavelength range from 850 nm to 1000 nm using a liquid nitrogen cooled CCD coupled to a Horiba iHR320 imaging spectrometer. The CCD (Horiba Symphony II) attached to the spectrometer has 26 µm square pixels and results in a typical spectral resolution

of 0.79 nm with the chosen grating of 300 lines/mm and a 500 nm blaze. The monochromator exit bandpass was 2 nm for collecting PL and 14 nm for RL emissions. For PL, the signal was integrated over a time period of 0.5 s and for RL over 30 s. The PL response was measured using 830 nm continuous-wave laser excitation. Two LP850 interference filters were placed in front of the spectrometer to reject emissions <850 nm. All obtained signals were corrected for the instrument response prior to further processing. Prior to fitting using up to three Gaussian peaks, emission spectra were converted from wavelength to energy space by multiplying the emission intensity with hc/E^2, where h is Planck's constant, c the speed of light and E the emission photon energy, following Hamilton et al. (1978) and Mooney and Kambhampati (2013). All recorded spectra were corrected for the instrumental background by subtracting the measurement obtained for an empty sample holder from the PL spectrum of each sample. For each sample, a PL measurement was performed on the bleached sample material prior to administering an X-ray dose. The first RL measurement was made immediately after turning on the X-ray source (which results in a maximum irradiation time of ~1 min of X-ray irradiation and thus the irradiation dose is estimated at ~3 Gy). Subsequent RL and PL emission spectra were measured once per hour, with irradiations up to 4 hours (~800 Gy), depending on the brightness of the sample. Measurements after different doses were performed to check for PL signal growth with dose, and RL signal decrease with increasing dose.

3.3 Excitation spectra

Excitation spectra were recorded on the same subsamples as the emission spectra after the samples were irradiated to doses ranging from 400 to 800 Gy, using the same X-ray source as described in section 3.2. Excitation spectra were measured at 7 K using COLUR. A Xe-lamp was used as an excitation source. Excitation wavelengths ranged from 460 nm to 820 nm for the 880 nm emission detection and from 495 nm to 912 nm for the 955 nm emission detection. A band pass of 3 nm was used for both excitation and emission monochromators and an integration time of 3 s was used for data collection. Excitation spectra were measured for emissions around ~880 nm (~1.41 eV, termed

190 $IRPL_{1.41}$) and ~955 nm (~1.30 eV, termed $IRPL_{1.3}$) using the same liquid nitrogen cooled CCD coupled
191 to a Horiba iHR320 imaging spectrometer as described in section 3.2. For recording $IRPL_{1.41}$ excitation
192 spectra two LP850 nm interference filters were placed in front of the spectrometer, and for $IRPL_{1.3}$
193 excitation spectra two LP925 interference filters were used. The emission was then recorded from
194 850 nm to 1000 nm for $IRPL_{1.41}$, and from 925 nm to 1000 nm for $IRPL_{1.3}$. From these three-
195 dimensional excitation-emission spectra the emission bands at 880 ± 5 nm ($IRPL_{1.41}$) and 955 ± 5 nm
196 ($IRPL_{1.3}$) were isolated and plotted as a function of excitation wavelength. The obtained spectra were
197 corrected for the excitation light flux of the Xe-lamp and the instrument response of the detection
198 unit. The data were converted from wavelength to energy space prior to fitting analysis following the
199 same approach as outlined for the RL and PL emission spectra in section 3.2.

200 **4 Results**

201 Here we describe the results obtained from IRPL and IR-RL emission spectroscopy and IRPL
202 excitation spectroscopy, by first comparing the optical resetting behaviour of the PL emissions and
203 then examining the potential influence of sample chemistry and structural state on IRPL and IR-RL
204 emissions and the electron trap emitting IRPL/IR-RL at 1.3 eV and 1.41 eV.

205 **4.1 IR-RL and IRPL emission spectra**

206 **4.1.1 General shape and optical resetting behaviour of the $IRPL_{1.3}$ and $IRPL_{1.41}$ emissions**

207 Emission spectra were recorded after different durations of X-ray irradiation. Representative
208 examples of the recorded IRPL emission spectra are shown in Figure 2, and all IRPL and IR-RL spectra
209 are displayed in Figure S1 in the supplementary material.

210 PL and RL emission spectra recorded for various samples show variations in signal intensities with
211 emission wavelength/energy. Generally, the spectra show their highest intensities either around
212 ~1.41 eV (~880 nm) or around ~1.3 eV (~955 nm) (see examples in Fig. 2). PL emission intensities
213 increase with increasing irradiation dose, whilst RL emission intensities decrease with increasing

irradiation dose. The rate of PL increase and RL decrease with increasing dose in the sample varies between samples and between emissions within a sample (cf. Fig. 2).

PL emission spectra recorded prior to switching on X-rays give information on the PL residual signal remaining after 18 hours of solar bleaching (see orange line in Fig. 2). The size of these residuals differs between samples; in some samples the PL signal is fully reset after 18 hours of solar bleaching (Fig. 2A for FSM-13LH), in others it is only partially reset (Fig. 2B for FSM-3) or even untouched (Fig. 2C for FSM-5). For samples FSM-13 (single phase microcline, 98.5 % K-feldspar), FSM-13LH (artificially disordered counterpart, Fig. 2A), FSM-6 (cryptoperthite, 74.4 % K-feldspar), FSM-6LH (artificially disordered counterpart) and CLBR (single phase albite, 0.5 % K-feldspar) the PL signal was reset to a lower level during bleaching (Fig. S1B, D, L, N and P). Interestingly, samples FSM-3 (cryptoperthite, 82.5 % K-feldspar, Fig. 2B) FSM-14 (cryptoperthite, 78.3 % K-feldspar) and FSM-5 (macroperthite, 74.8 % K-feldspar, Fig. 2C) showed a residual PL signal. For samples FSM-14 and FSM-5, the PL signal with an emission centred around 880 nm ($IRPL_{1.41}$) did not grow further with dose (Figs. 2C, S1H, J). The partially reset $IRPL_{1.41}$ in sample FSM-3 grows with dose, but not to the same extent as the $IRPL_{1.3}$ emission (Fig. 2B). The 18 hour solar simulator bleach reset the $IRPL_{1.3}$ in most samples, except for FSM-14 (Fig. S1H) and FSM-5 (Fig. 2C), where a residual remains.

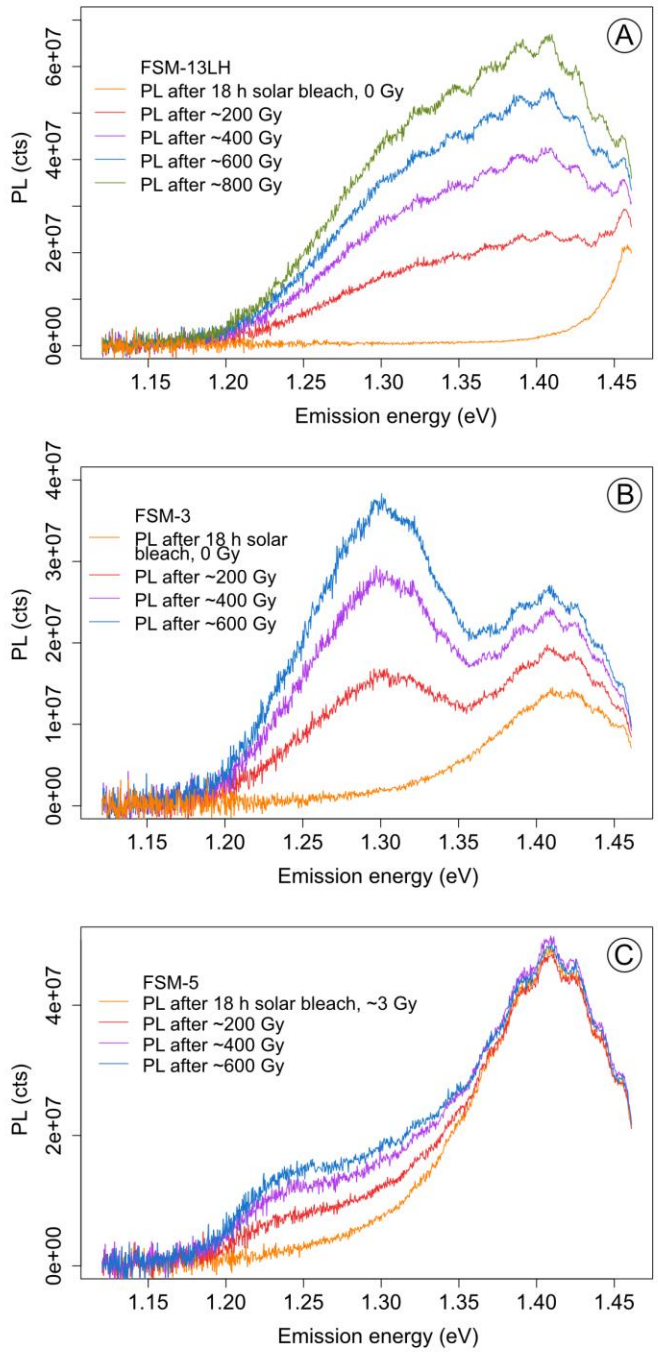

Fig. 2. Examples of IRPL emission spectra, which represent the range of spectra observed from our samples. Whilst the PL signal is reset to a background level (see orange curve recorded after 18 hours of solar simulator bleaching and before administering an X-ray dose) for FSM-13LH (A), the $IRPL_{1.3}$ (~955 nm) and $IRPL_{1.41}$ (~880 nm) signals reset to varying extent in the case of FSM-3 (B) and FSM-5 (C). The figures also show the different response of the three exemplary samples to X-ray doses of up to ~800 Gy, and how the two IRPL emissions grow differently with X-ray irradiation. It is particularly interesting that the $IRPL_{1.41}$ emission in FSM-5 does not bleach during 18 hours of exposure under in solar simulator and that this emission does not grow with increasing X-ray dose.

230

4.1.2 Intensities and energies of IRPL and IR-RL emissions

Kumar et al. (2018, 2020a) showed the presence of two IRPL and IR-RL emissions with peak maxima around 1.3 eV and 1.41 eV in their samples. In the present study the emission spectra were fitted in R using the *nls function* (Bates and DebRoy, 2018), which uses a non-linear least squares approach to iteratively find the most suitable fitting parameters for the given equation. A linear sum of *n* Gaussian peaks was fitted to the measured spectra, where *n* varied typically from 1 to 3. The best fit was determined by minimising the residuals while keeping *n* as small as possible. Equation 1 represents the fitted function, where *k* is a constant, *E* the emission photon energy (in eV), μ the mean energy of the Gaussian distribution (in eV) and σ the standard deviation (in eV). For each sample, the RL spectrum after a dose of ~3 Gy and the PL spectrum after the longest irradiation was chosen for fitting (Table 1). The measured emission spectra and corresponding fits are shown in Figure 3 for samples FSM-13, FSM-5 and CLBR. Emission spectra for all samples are shown in Figure S3.

$$f(E) = \sum_{i=1}^{n} k_i * exp\left(-\frac{1}{2} * \frac{(E_i-\mu_i)^2}{{\sigma_i}^2}\right) \quad [1]$$

The number of Gaussian peaks (*n*) used to describe the measured spectra varies across samples, but stays the same within one sample for RL and PL, with the exception of CLBR. The RL spectrum of CLBR (single phase albite, 0.5 % K-feldspar) can be fitted using two Gaussian functions with mean energies of 1.29 ± 0.05 eV and at 1.33 ± 0.03 eV (Fig. 3E). In contrast the PL spectrum of this sample can only be described by one Gaussian peak with a mean energy of 1.28 ± 0.05 eV (Fig. 3F). Single phase microcline sample FSM-13 shows RL and PL emission spectra that are described by a sum of two Gaussian peaks. In the RL spectrum of FSM-13, the emissions are centred around 1.33 ± 0.06 eV and around 1.42 ± 0.04 eV (Fig. 3A), whereas in the PL spectra the emissions are centred at 1.31 ± 0.05 eV and 1.43 ± 0.04 eV (Fig. 3B).

Perthitic samples FSM-3, FSM-14 and FSM-6 also show RL and PL spectra that can be described by two Gaussian peaks (Fig. S2). The peak positions of the emissions are similar to those recorded for FSM-13, with one emission being centred around 1.3 eV and the other around 1.41 eV (Table 1). The RL (Fig. 3C) and PL (Fig. 3D) emission spectra for FSM-5 are different to the other perthites, because they require three Gaussian peaks for fitting as opposed to two. In addition to RL and PL emissions around ~1.4 eV and ~1.3 eV, a third additional emission is recorded at 1.22 ± 0.02 and at 1.23 ± 0.03 eV for RL and PL, respectively (Fig. 3C, D).

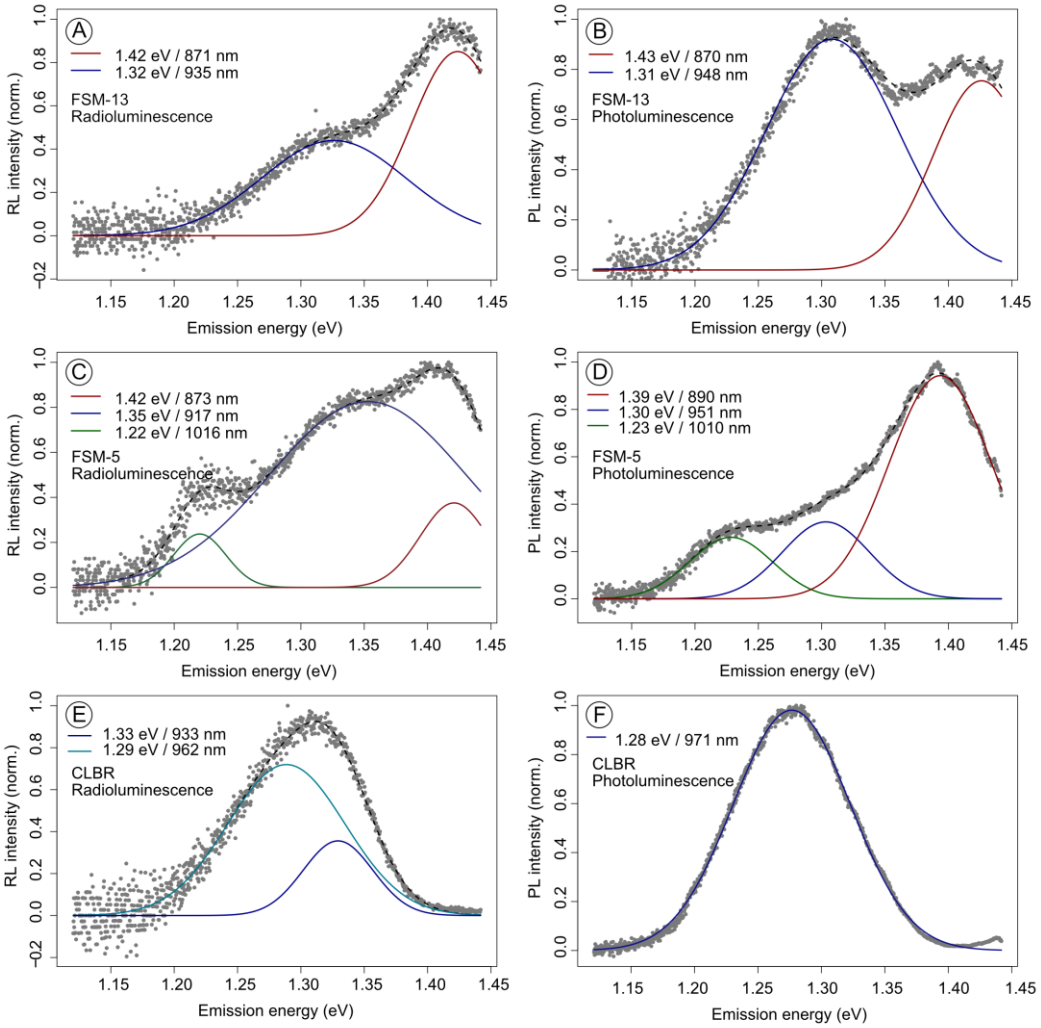

Fig. 3. Examples of radioluminescence (A, C, E) and photoluminescence (B, D, F) emission spectra of samples FSM-13 (A, B), FSM-5 (C, D) and CLBR (E, F). The recorded spectra were fitted using up to three Gaussian peaks. The mean of the distribution is given in the individual figures for both distributions. Further details of the fit are also presented in Table 1. RL and PL emission spectra of the other samples are shown in Figure S2 and results of the fitting of those spectra are also given in Table 1.

Table 1. Results of Gaussian fit of RL and PL emission spectra. K-FS (%) refers to the K-feldspar content calculated from oxide concentration obtained using XRF. Here, μ represents the mean energy (in eV) or wavelength (in nm) and sigma (σ) the standard deviation (in eV). K-FS (%) refers to the K-feldspar content calculated from oxide concentration obtained using XRF.

			RL				PL			
Sample ID	**K-FS (%)**	**Phases**	**μ (eV)**	**sigma (eV)**	**μ (nm)**	**Measured after a dose of**	**μ (eV)**	**sigma (eV)**	**μ (nm)**	**Measured after a dose of**
FSM-13	98.5	single phase microcline	1.33 1.42	0.06 0.04	935 871	~3 Gy	1.31 1.43	0.05 0.04	948 870	~800 Gy
FSM-13LH	98.5	disordered, but still single phase microcline	1.32 1.41	0.06 0.04	937 879	~3 Gy	1.32 1.42	0.06 0.04	936 875	~800 Gy
FSM-3	82.5	perthite (microcline and albite)	1.30 1.41	0.05 0.03	956 878	~3 Gy	1.30 1.42	0.05 0.03	954 876	~600 Gy
FSM-14	78.3	perthite (microcline and albite)	1.30 1.42	0.05 0.03	953 874	~3 Gy	1.32 1.41	0.06 0.03	941 877	~400 Gy
FSM-5	74.8	perthite (microcline and albite)	1.22 1.35 1.42	0.02 0.08 0.03	1016 917 873	~3 Gy	1.23 1.30 1.39	0.03 0.03 0.04	1010 951 890	~600 Gy
FSM-6	74.4	perthite (orthoclase and albite)	1.32 1.40	0.06 0.05	938 885	~3 Gy	1.31 1.40	0.05 0.05	945 887	~400 Gy
FSM-6LH	74.4	sanidine	1.26 1.38	0.04 0.06	982 899	~3 Gy	1.26 1.36	0.03 0.07	985 910	~400 Gy
CLBR	0.5	albite	1.29 1.33	0.05 0.03	962 932	~3 Gy	1.28	0.05	971	~200 Gy

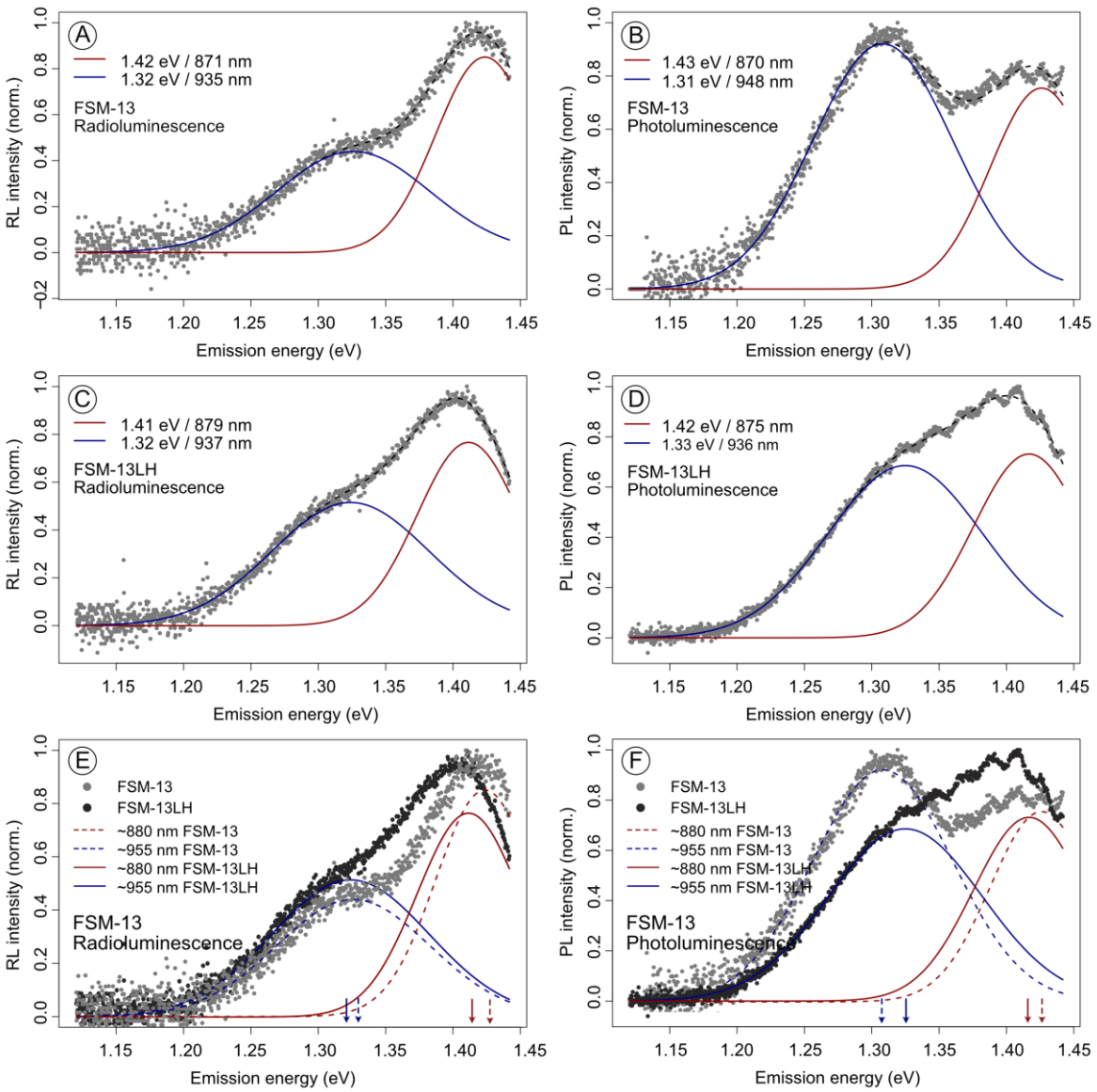

Fig. 4. Comparison of RL (A, C, E) and PL (B, D, F) emission spectra of FSM-13 (unheated material) and FSM-13LH (heated material). The emission spectra were fitted using two Gaussian peaks and the mean of the obtained distributions is given in the figures. Details of the fit are given in Table 1. Figures E and F show a comparison of the RL (E) and PL (F) emission spectra of the heated and unheated material. The dashed lines and light grey points correspond to the unheated material (FSM-13) and the solid lines and dark grey points to the heated material (FSM-13LH). The arrows pointing towards the x-axis show the change in emission peak position for the unheated (dashed line) and heated (solid line) material.

265

266 The effect of framework disorder on RL and PL emission spectra recorded in the infrared was tested
267 for two samples: one single phase microcline (FSM-13, referred to as FSM-13LH after heating) and

one perthite (FSM-6, referred to as FSM-6LH after heating, Figs. 4 and 5, respectively). Figure 4 shows the RL emission spectra for samples FSM-13 (Fig. 4A) and FSM-13LH (Fig. 4C) and both in direct comparison (Fig. 4E). The same is shown for PL emission spectra in Figures 4B, D and F, respectively. The RL emission spectrum of the heated sample FSM-13LH, compared to the unheated material (FSM-13) shows only very subtle changes in shape. Both emission peaks are present with similar relative intensities within the RL spectra of FSM-13 and FSM-13 LH (Fig. 4E). Fitting of the RL emission peaks results in mean emission energies of 1.33 ± 0.06 eV (FSM-13) and 1.32 ± 0.06 eV (FSM-13LH) and of 1.42 ± 0.04 eV (FSM-13) and 1.43 ± 0.04 eV (FSM-13LH). In contrast, PL of heated sample FSM-13LH, compared to FSM-13, shows changes in shape and in the relative intensities of the two identified emission maxima. Whilst in the PL spectrum of FSM-13 the $IRPL_{1.3}$ emission is more prominent, the $IRPL_{1.41}$ emission is the dominant emission of the heated sample FSM-13LH (Fig. 4F). The peak maxima are found at 1.31 ± 0.05 eV and 1.43 ± 0.04 eV for FSM-13 and at 1.32 ± 0.06 eV and 1.42 ± 0.04 eV for the heated sample FSM-13LH (Fig. 4F).

For FSM-6 and the heated material of FSM-6LH, a first visual examination of the shapes of the RL and PL emission spectra (Figs. 5E, F) does not indicate any significant changes, however, fitting analysis reveals differences in relative intensities and the mean energy of the subpeaks: In the case of RL (Fig. 5E) and PL (Fig. 5F), the relative intensity of the 1.3 eV subpeak decreases when comparing the unheated (FSM-6) to the heated material (FSM-6LH). Whilst the mean energy of this emission is found at 1.32 ± 0.06 eV in RL of FSM-6, it apparently shifts to 1.26 ± 0.04 eV in the spectrum of heated sample FSM-6LH (Fig. 5E). Similarly, in PL emission spectra of FSM-6 and FSM-6LH (Fig. 5F) the $IRPL_{1.3}$ emission occurs at 1.31 ± 0.05 eV and at 1.26 ± 0.03 eV, respectively. The higher energy subpeak at ~1.41 eV occurs at 1.40 ± 0.05 eV in RL of FSM-6 consistent with 1.38 ± 0.06 eV in FSM-6LH. Similarly, in PL this emission ($IRPL_{1.41}$) peaks at 1.40 ± 0.05 eV in FSM-6 (unheated) and at 1.36 ± 0.07 eV FSM-6LH (heated) (Fig. 5F).

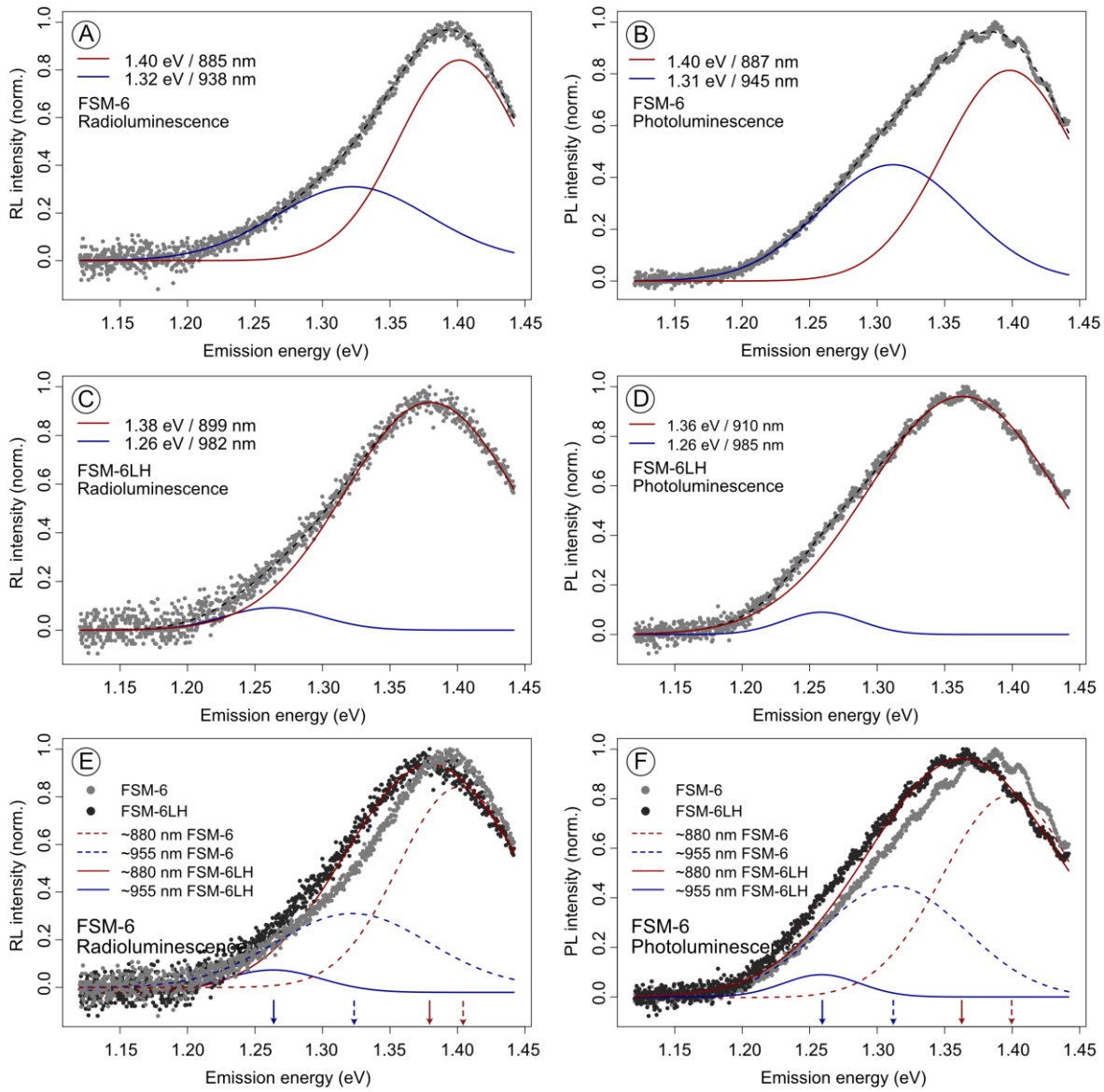

Fig. 5. Comparison of RL (A, C, E) and PL (B, D, F) emission spectra of FSM-6 (unheated material) and FSM-6LH (heated material). The emission spectra were fitted using two Gaussian peaks and the mean of the obtained distributions is given in the figures. Details of the fit are given in Table 1. Figures E and F show a comparison of the RL (E) and PL (F) emission spectra of the heated and unheated material. The dashed lines and light grey points correspond to the unheated material (FSM-6) and the solid lines and dark grey points to the heated material (FSM-6LH). The arrows pointing towards the x-axis show the change in emission peak position for the unheated (dashed line) and heated (solid line) material.

295 **4.2 Excitation spectra**

296 IRPL excitation spectra recorded from ~1.4 eV to ~2.6 eV for all samples reveal excitation peaks in
297 the infrared (~1.45 eV, peak 1 in Fig. 6A) and in the yellow to blue region (1.9 to 2.5 eV, peak 2 in Fig.
298 6) for $IRPL_{1.3}$ (955 ± 5 nm) and $IRPL_{1.41}$ (880 ± 5 nm) emissions, and additionally for the $IRPL_{1.2}$ (1030 ±
299 5 nm) emission in FSM-5 only. The excitation peak in the infrared was fully characterised for $IRPL_{1.3}$,
300 but not to its full extent for $IRPL_{1.41}$, due to instrumental limitations.

301 The excitation peak in the IR has first been observed in alkali feldspar excitation spectra recorded
302 with the emission in the UV by Hütt et al. (1988) and has been described as the IR resonance peak.
303 For the $IRPL_{1.3}$ eV excitation spectrum, this peak was initially reported by Prasad et al. (2017); they
304 proposed that this peak reflects a conduction band transition for trapped electrons. This peak is
305 marked as peak 1 and IR resonance peak in Figure 6A. Kumar et al. (2020a) described a second
306 excitation peak, denoted as peak 2, in IRPL excitation spectra of chemically different feldspars. The
307 range of excitation energies at which peak 2 was observed by Kumar et al. (2020a) overlaps with the
308 values of trap depth obtained using UV signals by Kars et al. (2013) and Riedesel et al. (2019) for a
309 range of chemically different feldspars. Based on the comparison with these earlier studies, and
310 measurements and analyses of an UV excitation spectrum of their samples, Kumar et al (2020a)
311 concluded that peak 2 in their IRPL excitation spectra reflects the electron transition from the
312 ground state of the electron trap to the conduction band and thus describes the trap depth of the
313 electron trap (Kumar et al., 2020a).

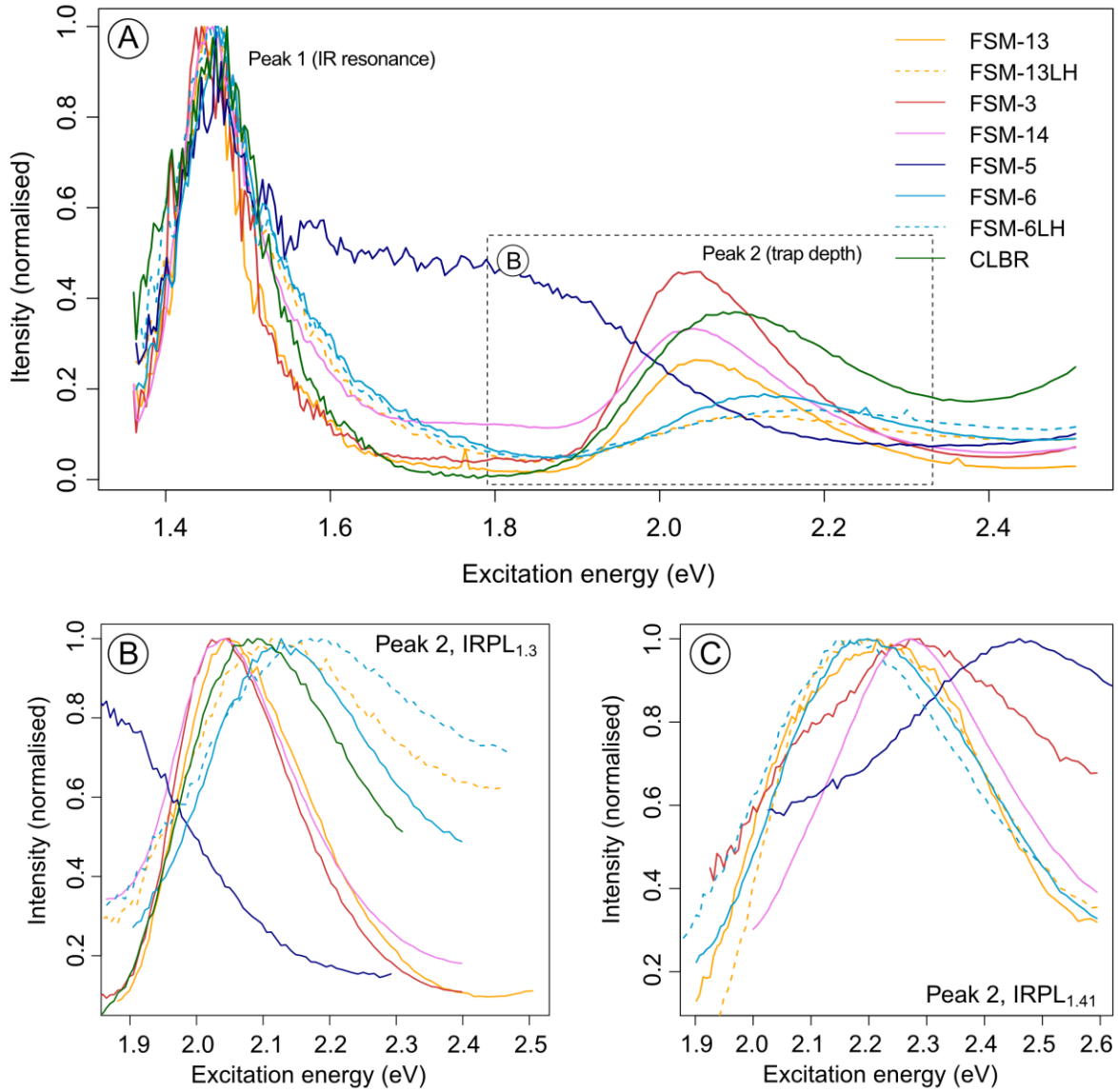

Fig. 6. A) Excitation spectra of all samples investigated recorded with excitation energies ranging from ~1.36 to ~2.51 eV. The emission was recorded at 1.3 eV ($IRPL_{1.3}$). Data have been normalised to the intensity of the IR resonance peak at ~1.45 eV. The dashed box indicates the excitation energy range isolated for B. B) Close-up of excitation peak 2 from $IRPL_{1.3}$ excitation spectra. C) Close-up of excitation peak 2 from $IRPL_{1.41}$ excitation spectra. The full $IRPL_{1.41}$ excitation spectra for all samples are shown in Fig. S3. Since single phase albite CLBR does not show an $IRPL_{1.41}$ emission, no excitation spectrum of this sample is displayed in C. Macroperthite FSM-5 also shows an emission at 1.2 eV, but for simplification excitation spectra recorded for this emission are not displayed in this figure, but can be found in Figure 7C and D.

314

315 **4.2.1 Trap depth**

316 Following the approach by Kumar et al. (2020a) we investigate sample-to-sample variations in shape
317 and position of excitation peak 2 to obtain information on the electron trap depths in the samples
318 investigated. Figure 6 enables a comparison between the position and shape of peak 2 of all samples
319 investigated, and Figure 7 allows a comparison of peak 2 recorded in $IRPL_{1.3}$ and $IRPL_{1.41}$ excitation
320 spectra for selected samples FSM-13, FSM-5 and CLBR. Excitation spectra for both emissions and all
321 samples are shown in Figure S3. In addition to qualitative descriptions, we quantify potential
322 variations in peak 2, and thus the trap depth, by selecting the excitation energy at which peak 2 has
323 its highest IRPL emission intensity. Since the spectra were recorded with a measurement resolution
324 of 2 nm, we are able to determine the peak position with a precision of at least ± 0.02 eV, since this
325 is the largest step in energy space observed from the excitation energy range measured. However,
326 this estimate is only based on the measurement resolution. To enable a comparison of the width of
327 the peaks, the full width half maximum (FWHM) of peak 2 was calculated and results are given in
328 Table 2 and Figure 10B.

329 Figures 6B and 6C show variations in the shape of peak 2 and in the position of the maximum
330 intensity. Peak 2 and thus the trap depth for $IRPL_{1.3}$ varies between 2.04 eV (FSM-13 and FSM-14)
331 and 2.20 eV (FSM-6LH), and from 2.16 eV (FSM-13LH) to 2.46 eV (FSM-5) for $IRPL_{1.41}$ (Table 2, Fig. 6B,
332 C). The width (FWHM) of peak 2 varies from 0.22 eV (FSM-3) to 0.53 eV (FSM-6LH) for $IRPL_{1.3}$ and
333 from 0.44 eV (FSM-14) to 0.63 eV (FSM-5) for $IRPL_{1.41}$ (Table 2, Fig. 6B, C).

334 The $IRPL_{1.3}$ excitation spectrum of single phase albite CLBR shows a trap depth of 2.09 eV (FWHM:
335 0.35 eV; Fig. 7F). No trap depth was calculated for the $IRPL_{1.41}$ emission, since the luminescence
336 recorded is identified as the tail of the $IRPL_{1.3}$ emission, thus a calculated trap depth would only
337 reflect the depth of the trap responsible for $IRPL_{1.3}$. Single phase microcline FSM-13 (Fig. 7A) has an
338 optical trap depth of 2.21 eV (FWHM of 0.47 eV) for $IRPL_{1.41}$ and a shallower trap depth of 2.04 eV
339 (FWHM of 0.24 eV) for $IRPL_{1.3}$.

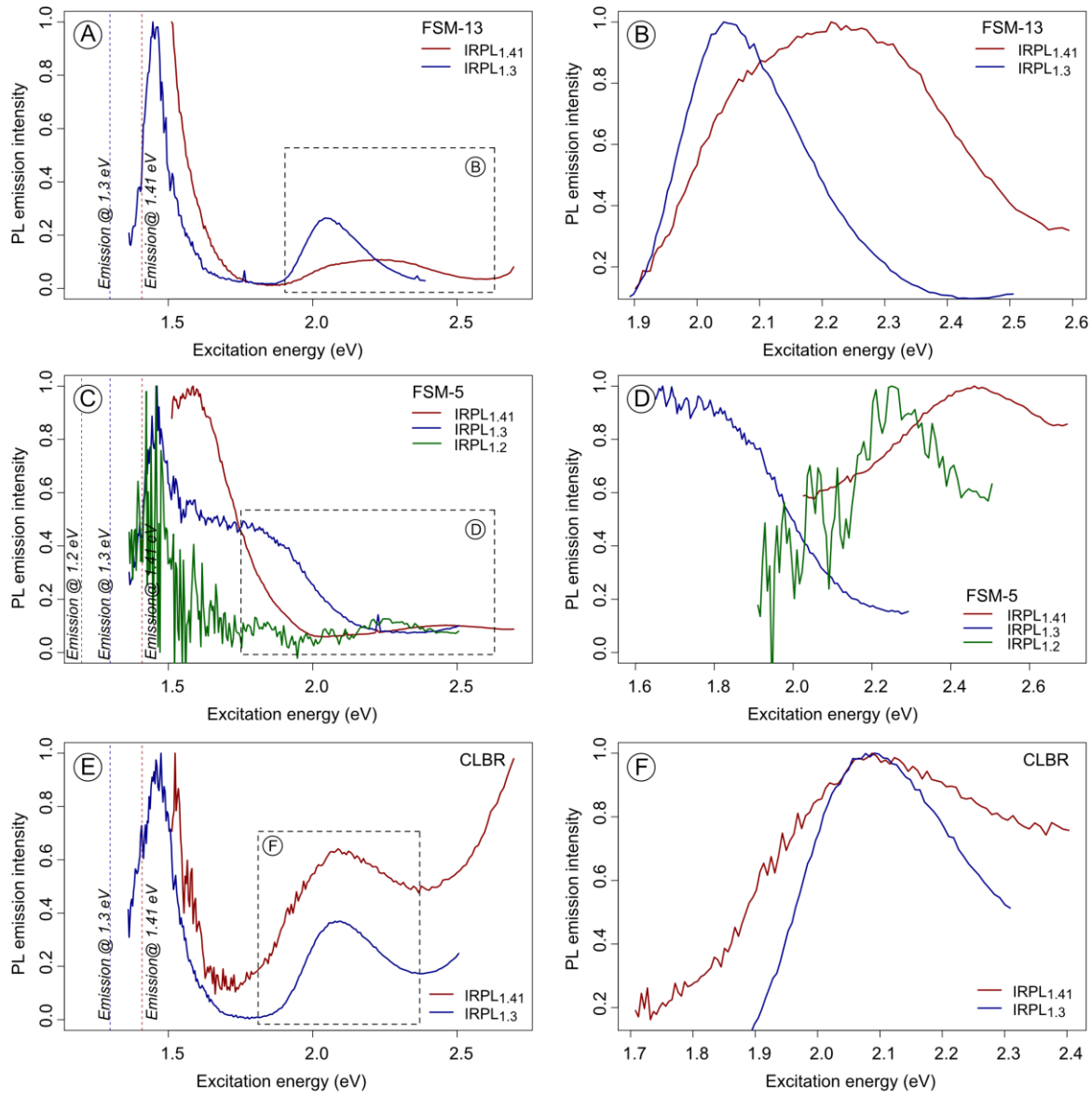

Fig. 7. Excitation spectra for the $IRPL_{1.41}$ and $IRPl_{1.3}$ nm emissions of samples FSM-13 (A, B), FSM-5 (C, D) and CLBR (E, F). The graphs were normalised to the point of highest signal intensity. For figures B, D and F, excitation peak 2 was isolated and normalised separately. These graphs were used to obtain the trap depth, by picking the point of highest intensity for the individual curves. The thus obtained mode (in eV and µm) are given in Table 2 for all samples and excitation spectra measured for all samples can be found in Figure S3. The emission window is indicated in A, C and E with dashed vertical lines.

340

341 All perthitic samples show a similar pattern as FSM-13, where the trap depth is shallower for $IRPL_{1.3}$,
342 compared to $IRPL_{1.41}$ (Table 2, Figure 10B). In the perthitic samples the trap depth for $IRPL_{1.41}$ ranges
343 from 2.20 eV in FSM-6 (FWHM of 0.47 eV, Figs. 9B, D) to 2.46 eV in FSM-5 (FWHM of 0.63 eV, Figs.

7C, D) and for $IRPL_{1.3}$ from 2.05 eV (FSM-3, FWHM of 0.22 eV) to 2.13 eV (FSM-6, FWHM of 0.42 eV). Macroperthite FSM-5 does not show a peak between 2 eV and 2.5 eV in $IRPL_{1.3}$ excitation spectra, but rather a shoulder on the IR resonance peak is seen which stretches up to ~2.1 eV (Fig. 7C). Thus, a trap depth cannot be defined for the $IRPL_{1.3}$ centre of FSM-5. FSM-5 is also different to other samples because a third emission ($IRPL_{1.2}$) was found in the excitation spectra of FSM-5 (Fig. 7C and D). Although the spectrum is less intense for an emission at 1.2 eV, both excitation peaks are recognisable and fully characterised. Excitation peak 2 occurs at lower excitation energy (2.25 eV) in case of $IRPL_{1.2}$, compared to $IRPL_{1.41}$, where a trap depth of 2.46 eV is measured.

The $IRPL_{1.3}$ and $IRPL_{1.41}$ excitation spectra of the two samples used in the heating experiment (FSM-13LH and FSM-6LH; see section 3.1 for details) show subtle changes compared to the excitation spectra of the unheated counterparts (single phase microcline FSM-13 and perthite FSM-6, cf. Figs. 8 and 9). Figure 8 shows the excitation spectra of heated sample FSM-13LH, in comparison to the unheated sample material (single phase microcline FSM-13). The $IRPL_{1.41}$ excitation spectra of FSM-13 and FSM-13LH are similar, with a slight shift of the entire excitation spectra towards lower energy from the ordered specimen FSM-13 to the disordered sample FSM-13LH (Fig. 8A). Trap depths associated with the $IRPL_{1.41}$ emission are 2.21 eV for FSM-13 compared to 2.16 eV for FSM-13LH (Fig. 8B). In case of the $IRPL_{1.3}$ excitation spectra of FSM-13 and FSM-13LH the obtained trap depths are 2.04 eV (FSM-13) and 2.11 eV (FSM-13LH, Fig. 8D), respectively, and the FWHM changes from 0.24 eV in the unheated sample FSM-13 to 0.50 eV in the heated sample FSM-13LH. Additionally, a change in relative intensity between the IR resonance peak and excitation peak 2 is observed for $IRPL_{1.3}$: peak 2 has an intensity of ~30 % and ~10 % of the corresponding IR resonance peaks in the unheated and heated materials, respectively.

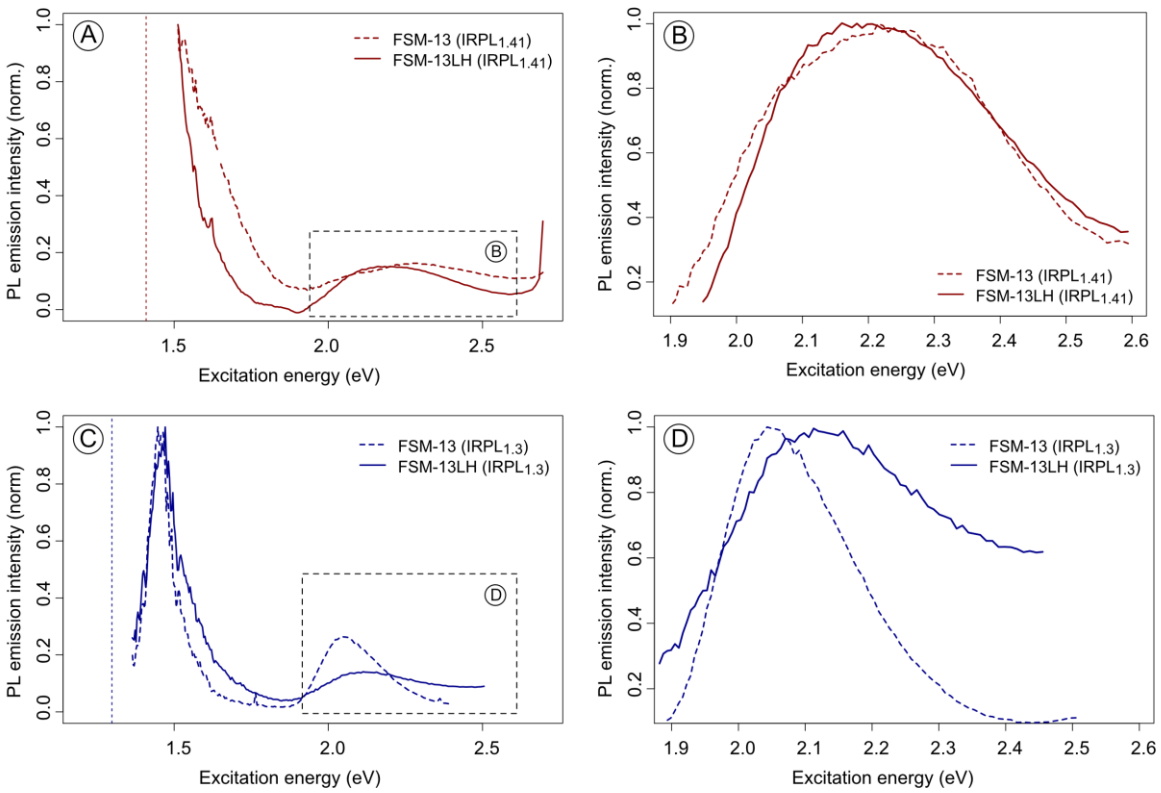

Fig. 8. Excitation spectra of samples FSM-13 (unheated material, dashed line) and FSM-13LH (heated material, solid line) in comparison for the $IRPL_{1.41}$ emission A and B) and the $IRPL_{1.3}$ emission (C and D). A and C show the complete excitation spectra measured for both samples and both emissions. The graphs were normalised to the highest intensity. B and D focus on a comparison of excitation peak 2. For these two graphs this excitation peak was isolated and then the spectra were normalised to the highest intensity.

366

367 The comparison of $IRPL_{1.3}$ and $IRPL_{1.41}$ excitation spectra measured for perthitic sample FSM-6 and
368 the heated material of FSM-6LH are shown in Figure 9. Whilst the IR resonance peak for $IRPL_{1.3}$ and
369 $IRPL_{1.41}$ remains largely identical between the heated and unheated sample material, excitation peak
370 2 changes slightly for both emissions recorded. The maximum of peak 2 in the $IRPL_{1.41}$ excitation
371 spectra is recorded at 2.20 eV for FSM-6 and at 2.18 eV for FSM-6LH (Fig. 9B). For the $IRPL_{1.3}$
372 emission the position of the highest intensity of peak 2 is recorded at 2.13 eV for FSM-6 and at
373 2.20 eV for FSM-6LH. Additionally, peak 2 is 0.11 eV wider in case of $IRPL_{1.3}$ excitation spectra of
374 FSM-6LH compared to FSM-6 (Fig. 9D).

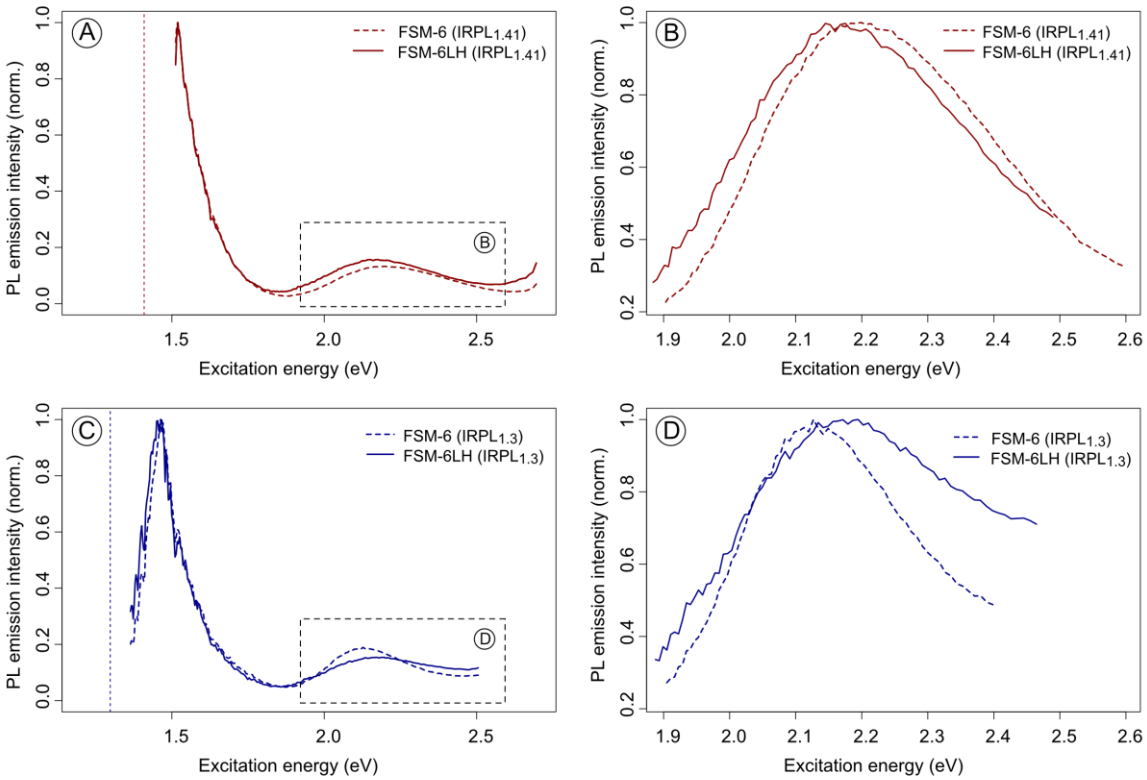

Fig. 9. Excitation spectra of samples FSM-6 (unheated material, dashed line) and FSM-6LH (heated material, solid line) in comparison for the $IRPL_{1.41}$ emission (A and B) and the $IRPL_{1.3}$ emission (C and D). A and C show the complete excitation spectra measured for both samples and both emissions. The graphs were normalised to the highest intensity. B and D focus on a comparison of excitation peak 2. For these two graphs this excitation peak was isolated and then the spectra were normalised to the highest intensity.

375

376

Table 2. Results of excitation spectra with emissions recorded at ~880 nm ($IRPL_{1.41}$) and ~955 nm ($IRPL_{1.3}$). K-FS (%) refers to the K-feldspar content calculated from oxide concentration obtained using XRF. The relative feldspar compositions were obtained using stoichiometry. E_t refers to the transition from the ground state of the electron trap to the edge of the conduction band. Data for R28 and K8 are from Kumar et al (2020a). [1]The association of R28 as orthoclase is solely based on information given in Poolton et al. (2009), however, these authors do not present any analytical data (i.e. XRD or related).

Sample ID	K-FS (%)	Details	1.41 eV (880 nm) emission		1.3 eV (955 nm) emission				1.2 eV (1030 nm) emission	
			E_t (eV)	FWHM (eV)	IR res. (eV)	FWHM (eV)	E_t (eV)	FWHM (eV)	Et (eV)	FWHM (eV)
FSM-13	98.5	single phase microcline	2.21	0.47	1.46	0.08	2.04	0.24	NA	NA
FSM-13LH	98.5	slightly disordered single phase microcline	2.16	0.47	1.46	0.14	2.11	0.50	NA	NA
FSM-3	82.5	perthite (microcline and albite)	2.29	0.62	1.45	0.11	2.05	0.22	NA	NA
FSM-14	78.3	perthite (microcline and albite)	2.27	0.44	1.45	0.12	2.04	0.25	NA	NA
FSM-5	74.8	perthite (microcline and albite)	2.46	0.63	1.46	0.15	NA	NA	2.25	0.36
FSM-6	74.4	perthite (orthoclase and albite)	2.20	0.47	1.46	0.13	2.13	0.42	NA	NA
FSM-6LH	74.4	sanidine	2.18	0.51	1.47	0.14	2.20	0.53	NA	NA
CLBR	0.5	albite	NA	NA	1.46	0.15	2.09	0.35	NA	NA
R28	95	orthoclase[1]	2.31		1.46		2.15		NA	NA
K8	84	microcline perthite (Baril, 2004)	2.18		1.46		2.09		NA	NA

4.2.2 IR resonance peak

The IR resonance peak is thought to reflect an excited state of an electron trapping centre in feldspar (Hütt et al., 1988; Bailiff and Poolton, 1991; Poolton et al., 1995). The IR resonance peak is fully characterised in $IRPL_{1.3}$ excitation spectra of all samples, which allows for a quantification of the resonance energy, by selecting the IR resonance peak maximum and by calculating the FWHM of this peak (Table 2). For this purpose, the data was smoothed by calculating a running average of three data points. From the smoothed data the maximum peak intensity was selected as peak position and the FWHM of the smoothed peak was calculated (Table 2). A direct sample-to-sample comparison of the IR resonance peak (unsmoothed data) shows only little variation in the shape and peak position (Fig. 6A), compared to the variation observed for excitation peak 2 for $IRPL_{1.3}$ excitation spectra (Fig. 6B) and $IRPL_{1.41}$ excitation spectra (Fig. 6C). Also, from the smoothed data the identified IR resonance peak position varies from 1.45 eV (FSM-3, FSM-14) to 1.47 eV (FSM-6LH) and the FWHM varies from 0.08 eV (FSM-13) to 0.15 eV (CLBR).

5 Discussion

Previous studies have suggested different locations for electron trapping centres in feldspars: substitution of Pb^{2+} for K^{+} on M sites (Erfurt, 2003), occupancy of tetrahedral sites of the Si,Al-framework (Short, 2004), or occupancy of an unknown lattice site, but located in two different crystallographic environments (Kumar et al., 2018, 2020a). However, these studies were conducted on a limited number of feldspar samples, covering a narrow chemical range, or on grain mixtures extracted from sediment, which likely contain grains of different geological origin and different chemical composition. With this paper and the samples investigated we contribute to the growing body of knowledge on electron trapping centres in feldspars by investigating a suite of single crystal feldspars that span the entire alkali feldspar solid solution, including K- and Na-feldspar end members, and the results are discussed below.

406 **5.1 Sample-dependent variations in IRPL and IR-RL emission spectra**

407 Erfurt (2003) and Erfurt and Krbetschek (2003) observed IR-RL emissions at 1.36 eV (910 nm) and at
408 1.43 eV (865 nm) in a single crystal feldspar and in feldspars extracted from sediment. Kumar et al.
409 (2018) measured emission energies of 1.3 eV (955 nm) and 1.41 eV (880 nm) in the IR-RL and IRPL
410 emission spectra of their alkali feldspars in single crystal feldspars and sediment extracts. IR-RL and
411 IRPL emission energies measured in this paper are within the range of emission energies observed
412 by Erfurt (2003), Erfurt and Krbetschek (2003) and Kumar et al. (2018, 2020a), but slightly more
413 consistent with the results of Kumar et al. (2018, 2020a). This closer agreement with the results in
414 the present study and those by Kumar et al. (2018, 2020a) might indicate a slight dependency of the
415 measurement results on the measurement conditions; the instrument used here is the same as used
416 by Kumar et al. (2018, 2020a).

417 Our IRPL and IR-RL emission spectra show that emissions centred around 1.3 eV are present in all
418 samples investigated. Similar observations were made for the IRPL and IR-RL emissions centred
419 around 1.41 eV, except the emission is absent in our only single phase albite CLBR (which only
420 contains 0.5 % K-feldspar). The IR-RL emission spectrum of CLBR can be fitted using the sum of two
421 Gaussian peaks, however both fitted Gaussian distributions are centred around 1.3 eV (Table 1, Fig.
422 3E). The IRPL emission spectrum of CLBR can only be described with a single Gaussian function
423 centred at ~1.3 eV (Table 1, Fig. 3F). It is interesting to note that both of the ordered single phase
424 samples (FSM-13 and CLBR) show an IRPL and IR-RL emission centred around 1.3 eV, but only the
425 ordered single phase microcline (FSM-13) shows an emission at ~1.41 eV (cf. Fig. 3A, B and Fig. 3E,
426 F). The difference between these two ordered single phase single crystal feldspars is their chemical
427 composition: Whilst single phase microcline sample FSM-13 contains 98.5 % K-feldspar, single phase
428 albite (CLBR) contains only 0.5 % K-feldspar; this potentially suggests that the 1.3 eV emission is
429 independent of the cation on M sites in the crystal, whereas the 1.41 eV emission might be linked to
430 the presence of K^+ ions on M sites. However, we can only base this on the measurement of these

two alkali feldspar end member samples and further research is necessary to validate our results. Additionally, it should be noted here that, in contrast to our results, Kumar et al. (2020b), who used a cathodoluminescence attachment to a scanning electron microscope, found that cathodoluminescence emissions in the IR at ~1.3 eV increase with increasing K-content of the grain measured, however, the exact mineral phases probed are unknown. Despite contradictory trends, results by Kumar et al. (2020b) and presented here indicate that the suggestion by Erfurt (2003) of electron trapping centres being created on M sites due to the substitution of K^+ ions by Pb^{2+} ions might not hold true. Both Kumar et al. (2020b) and we in this present study show that at least one IRPL emission is independent of the M site cation occupancy, whilst Erfurt (2003) linked both emissions to two excited states of the same defect type on M sites. Our results are in addition to previous work (e.g. Kumar et al. 2018, 2020a), which already indicated that the same type of defect, but in two different crystallographic environments gives rise to the IRPL emissions. It is also interesting to note that macroperthite FSM-5 (74.8 % K-feldspar) is the only sample which shows an additional PL and RL emission at ~1.2 eV, which also indicates that additional factors, other than the M site cation occupancy, influence electron trapping centres in feldspars.

Mean IRPL and IR-RL emission energies for the fitted Gaussian peaks are similar across the sample suite investigated and, in most cases, IRPL and IR-RL emissions occur at similar emission energies. The only exception is CLBR, where the RL emission can be described by a sum of two Gaussian, whilst the PL emission is only described by a single Gaussian peak (Table 3, Fig. 10C, D). Furthermore, even in the case of the unheated and heated sample pairs, only small changes in emission peak energy were observed (Fig. 4 for FSM-13/FSM-13LH, Fig. 5 for FSM-6/FSM-6LH). An absolute comparison of IRPL signal intensities of the unheated and heated sample pairs cannot be conducted, because it was not possible to fix an exact sample mass on the cold finger. However, even when comparing the IRPL intensities of FSM13/FSM-13LH and FSM-6/FSM-6LH (data not shown) no obvious variations in signal intensities for the heated/unheated sample pairs could be observed. This suggests that the IRPL and IR-RL emissions centred at 1.3 eV and 1.41 eV are largely unaffected by

457 changes to the tetrahedral site occupancy of Al^{3+} ions. In contrast, disordering Al^{3+} ions on the
458 framework of the same samples FSM-13LH and FSM-6LH resulted in a significant increase of the blue
459 luminescence emission (~410 nm), a change in the TL curve shape, particularly of the blue emission,
460 and increased the fading rate of the blue IRSL signal (Riedesel et al., 2021). Thus, it appears that
461 whilst the recombination centres related to the blue emission are highly affected by framework
462 disorder, most likely due to their location on Al-O-Al bridges (Finch and Klein, 1999; Riedesel et al.,
463 2021), the electron trapping centres seem to be relatively independent from the degree of
464 framework disorder in feldspars.

465 Since the IRPL signal is intended for use in luminescence dating, the optical resetting of the $IRPL_{1.3}$
466 and $IRPL_{1.41}$ emissions is of importance for studies constraining the feldspar sample's last exposure
467 to light. Kumar et al. (2020a) analysed a single feldspar sample separated from sediment (R47) and
468 found that irrespective of the light source used for bleaching (405 nm, 470 nm or 880 nm LEDs, or a
469 SOL2 solar simulator), the IRPL emission centred around ~1.41 eV depletes more slowly than the
470 emission around 1.3 eV. After 24 hours exposure to the SOL2, their signals had fallen to ~5% for the
471 1.3 eV emission and between 5 % and 10 % for the ~1.41 eV emission. Duller et al. (2020) also
472 studied bleaching of the $IRPL_{1.3}$ signal. They used feldspars separated from a dune sand and found
473 that the $IRPL_{1.3}$ signal fell to ~3 % after bleaching using a 1 W 365 nm LED for 5.5 hours. From our
474 experiments it is evident that the two IRPL emission peaks respond differently to solar simulator
475 bleaching. Whilst the $IRPL_{1.3}$ emission (and the $IRPL_{1.2}$ emission for sample FSM-5) is completely reset
476 by an 18 hour solar simulator bleach for most samples (Figs. 2A, S1), the extent to which the $IRPL_{1.41}$
477 emission bleaches varies significantly between samples (Fig. 2B, C). These results suggest that the
478 extent of IRPL signal depletion is sample dependent, and this may have significant implications for
479 the application of IRPL for dating and strengthen the need for single grain IRPL analyses (Duller et al.
480 2020). However, further and more detailed bleaching experiments of chemically and structurally
481 well-constrained samples are necessary to be able to link variations in signal depletion with physical
482 properties of the samples.

5.2 Variations in excitation spectra of alkali feldspars

Our $IRPL_{1.3}$ and $IRPL_{1.41}$ excitation spectra revealed differences in the position of excitation peak 2, which was interpreted as reflecting the trap depth following Kumar et al. (2020a). For all our samples we observed a larger trap depth related to the $IRPL_{1.41}$ emission, compared to the $IRPL_{1.3}$ emission. The trap depth of the $IRPL_{1.3}$ trapping centre varies from 2.04 eV (FSM-13 and FSM-14) to 2.20 eV (FSM-6LH) and for the $IRPL_{1.41}$ trapping centre from 2.16 eV (FSM-13LH) to 2.46 eV (FSM-5). The trap depths obtained here are similar to those measured by Kumar et al. (2020a). These authors also observed smaller trap depths for the $IRPL_{1.3}$ centre compared to the $IRPL_{1.41}$ centre and respective trap depths varied from 1.90 eV to 2.21 eV and from 2.18 eV to 2.38 eV, for $IRPL_{1.3}$ and $IRPL_{1.41}$, respectively. When comparing our $IRPL_{1.3}$ and $IRPL_{1.41}$ trap depth values and those presented by Kumar et al. (2020a), we do not observe any trends in trap depth with chemistry of the samples, e.g. K-feldspar content (Fig. 10B, Table 2). However, the absence of the $IRPL_{1.41}$ emission in our single phase albite CLBR (0.5 % K-feldspar) potentially suggests that the $IRPL_{1.41}$ trapping centre is related to the presence of K^+ ions on M sites and that a certain number of K^+ ions have to occupy M sites to enable the presence of the $IRPL_{1.41}$ trapping centre in feldspars.

Artificial framework disorder (produced by laboratory heating of a sub-sample of samples FSM-13LH and FSM-6LH) influences the trap depth of both centres slightly, and in both samples the $IRPL_{1.3}$ trapping centres seems to be affected more, compared to the $IRPL_{1.41}$ trapping centre (Fig. 8B, C and Fig. 9B, C). Additionally, the FWHM of excitation peak 2 increases in the heated samples (FSM-13LH and FSM-6LH) compared to the unheated material (FSM-13 and FSM-6, Fig. 8 and 9), especially in the case of $IRPL_{1.3}$ excitation spectra. Since the rising limb of the peak was suggested to be related to the optical transitions in the band tail states (Prasad et al., 2017; Kumar et al., 2020a), the increase in the peak width for the heated samples may suggest that disordering the Al,Si-framework changes the band tail width. This interpretation is consistent with the suggestion of band tail states being associated with variations in bonding angles in the lattice (Poolton et al., 2002a). Artificial

disordering of the framework in our samples potentially influences the bonding angles within the crystal and results in a change in symmetry as a consequence of the re-distribution of Al^{3+} ions within the crystal (e.g. Goldsmith and Laves, 1954; Stewart and Ribbe, 1969; Deer et al., 2013, p. 256-257). The presence of sub-conduction band-tail states could also explain why excitation peak 2 is much wider, compared to the width of the IR resonance peak (cf. Table 2). Additionally, it could be considered that the large width of peak 2 could potentially reflect a distribution of ground state energies for this type of electron trapping centre. It has been argued previously that luminescence from feldspars arises due to a distribution of ground state energies of electron trap(s) (e.g. Strickertsson, 1985; García-Guinea et al., 2003), however, these suggestions are mainly based on analyses of thermoluminescence curve shapes.

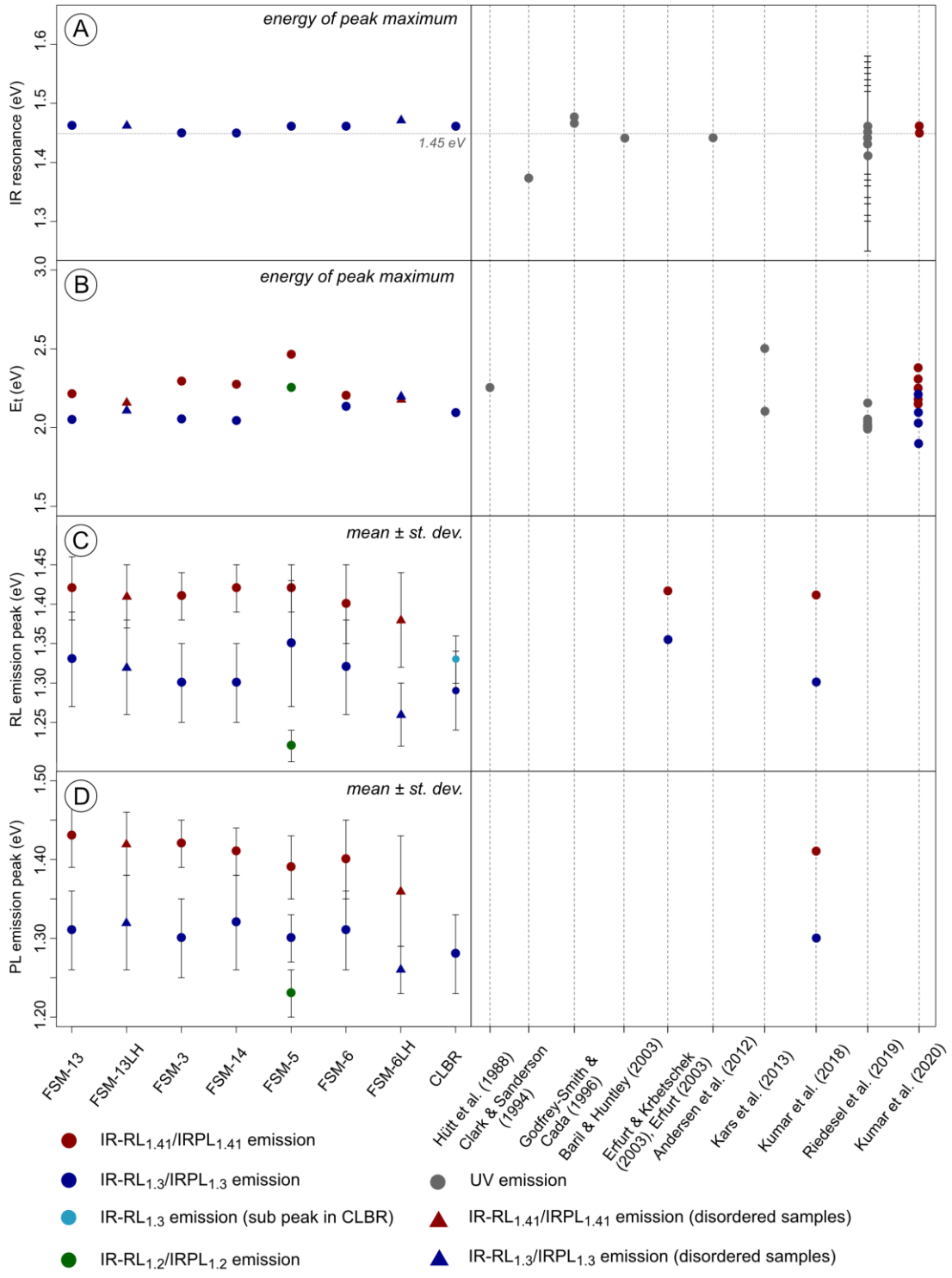

Fig. 10. Summary figure of results presented in this paper in comparison with selected published results. For Hütt et al. (1988), Baril and Huntley (2003) and Andersen et al. (2012) examples of their experimental results were picked (n = 1). Baril and Huntley (2003) and Andersen et al. (2012) fitted the IR resonance peak in their excitation spectra with various equations or multiple Gaussian distributions. Thus. a comparison of the numerical values obtained by these authors and the data measured in the present paper is difficult. For this reason only examples of one sample each were picked and uncertainties are not displayed in the case of Baril

and Huntley (2003) and Andersen et al. (2012). For Clark and Sanderson (1994) only their measurement of F1 reference feldspar using a halogen lamp is displayed. Godfrey-Smith and Cada (1996) identify the IR resonance peak centred around 840 nm (~1.48 eV) in nearly pure Na-feldspar end members and around 845 nm (~1.47 eV) in microcline, plagioclase and in feldspars extracted from sediments.

The data points related to Kars et al. (2013, n = 2) and Riedesel et al. (2019, n = 17) are based on fitting a rising continuum in excitation spectra using the equation for the photo-ionisation cross-section (Bøtter-Jensen et al., 2003). Kars et al. (2013) did not provide uncertainties for their trap depth values. The uncertainties provided on the trap depth by Riedesel et al. (2019) represent only uncertainties on the fit, not on the trap depth. Riedesel et al. (2019) fitted the IR resonance peak with a single Gaussian distribution, subsequently the values presented in this figure represent the mean and standard deviation of this fit. Kumar et al. (2020a) obtained the trap depth for the excitation spectra recorded in the infrared by picking the highest point of a specific excitation peak (n = 6). These authors provide an uncertainty of 0.02 eV on all trap depth values. For the IR resonance peak position Kumar et al. (2020a) give results for the emission recorded at 1.3 eV. No uncertainties on the peak position of the six samples investigated are given.

Beside the trap depth, $IRPL_{1.3}$ excitation spectra also reveal information on the IR resonance peak. From $IRPL_{1.3}$ excitation spectra we obtained the IR resonance peak position with a mean energy of 1.46 ± 0.01 eV. These results are in good agreement with previous work (e.g. Fig. 10A; Hütt et al., 1988; Clark and Sanderson, 1994; Godfrey-Smith and Cada, 1996; Baril and Huntley, 2003; Andersen et al., 2012; Riedesel et al., 2019). In accordance with Bøtter-Jensen et al. (1994) we observed similar IR resonance peak positions and shapes for the K- and Na-feldspar end members.

Interestingly, whilst we observed changes in trap depth between samples, the IR resonance peak is invariant between samples (Figs. 6A and 10A, Table 2). Assuming a simple hydrogen model (eq. 2a) to be applicable for feldspars, Poolton et al. (2002b) predicted a ground state energy (n = 1) of 1.97 eV from the conduction band edge and a transition from the ground state to the excited state (1s -> 2p optical transition) of 1.48 ± 0.04 eV, both of which are based on the same variables for the effective electron mass ($m_e^* = (0.79 \pm 0.02)m_e$, Poolton et al., 2001) and the relative permittivity of the material of $\varepsilon_r = 2.33$ (for Na-feldspar end member, Keller, 1966).

$$E_n = -\frac{2\pi^2 m_e^*}{h^2}\left[\frac{e^2}{4\pi\epsilon_0\epsilon_r}\right]^2\left(\frac{1}{n^2}\right) \quad [2a]$$

For a given trap depth, we can predict the excited state (n = 2) in our samples using equation 2a. The first part of equation 2a $\left(\frac{2\pi^2 m_e^*}{h^2}\left[\frac{e^2}{4\pi\epsilon_0\epsilon_r}\right]^2\right)$ represents the trap depth (E_t). Thus, equation 2a can be rewritten as:

$$E_n = -E_t\left(\frac{1}{n^2}\right) \quad [2b]$$

As an example: FSM-6 ($IRPL_{1.3}$ centre) has a trap depth of E_t = 2.13 eV and an IR resonance peak at 1.46 eV. Using equation 2b and E_t = 2.13 eV (n = 1), the excited state (n = 2) is calculated to be located at 1.60 eV above the ground state. The discrepancy of 0.14 eV between model predictions and experimental observation could either indicate the limitation of this simple model to extract precise energies, and/or the limitation of our interpretation of peak 1 and peak 2 in terms of the excited and ground state of the trap. In addition to developing a refined model, resolving this discrepancy requires a better understanding of whether peak 2 represents a single trap depth or a distribution of trap depths where each defect is influenced by its local crystal field. Further investigations of this aspect necessitate spatially resolved excitation spectra measurements, ultimately at the scale of a single defect. IRPL because of its non-destructive nature potentially makes such measurements possible for the first time.

6 Conclusions

In this paper we investigated potential causes of variations seen in IRPL and IR-RL emission spectra and in IRPL excitation spectra of chemically and structurally different single crystal alkali feldspars. We applied the novel site-selective method of IRPL excitation-emission spectroscopy (Kumar et al., 2020a) to link occurrences and characteristics of the two IRPL trapping centres ($IRPL_{1.3}$ and $IRPL_{1.41}$ trapping centre) with mineralogical properties of the samples.

For our chemically and structurally different samples we observed IRPL and IR-RL emissions at 1.2 eV, 1.3 eV and at 1.41 eV; the mean emission peak energies are observed to be similar for both IR-RL and IRPL within any individual sample. However, there are sample-dependent variations in the

number of emission peaks and their energies, as well as in the trap depth of the $IRPL_{1.3}$ and $IRPL_{1.41}$ centres. Our results suggest that the $IRPL_{1.41}$ trapping centre and related $IRPL_{1.41}$ and $IR\text{-}RL_{1.41}$ emissions may be linked to the presence of K^+ ions on M sites in the feldspar crystal lattice. In contrast, the $IRPL_{1.3}$ trapping centre seems to be independent of the chemical composition of the crystal, likely excluding M sites as potential host lattice sites for electron trapping centres in feldspars. Whilst previous research on the same samples revealed significant changes to the blue luminescence emission and its fading rate due to artificial disordering of the framework (Riedesel et al., 2021), IRPL and IR-RL emissions explored in the present study seem to be largely independent of changes to the distribution of Al^{3+} ions on the Al,Si-framework. Thus, unlike the recombination centres participating in the blue luminescence emission (~410 nm) (Speit and Lehmann, 1982b; Finch and Klein, 1999; Riedesel et al., 2021), the crystal defects acting as the electron trapping centres are probably not located on Al-bridging O ions. A comparison of IRPL and IR-RL emissions of single phase feldspars and perthites do not reveal any relationships between phases present in a single crystal and number of IRPL or IR-RL emission peaks or their positions.

We observed sample-to-sample variations in the extent to which the $IRPL_{1.3}$ and $IRPL_{1.41}$ emissions reset optically. Residual $IRPL_{1.41}$ emissions after 18 hours of solar simulator bleaching indicate that the degree of IRPL signal depletion is sample dependent, and this may have significant implications for the use of IRPL in luminescence dating.

Acknowledgements

SR would like to thank Aberystwyth University for funding her PhD research through an AberDoc PhD scholarship (Aberystwyth University). SR would like to thank Andrew Brown (Aberystwyth University) for laboratory assistance during the heating experiments. We thank Prof Javier Garcia-Guinea (Museo Nacional de Ciencias Naturales, Madrid) and Prof Adrian A. Finch (University of St.

Andrews) for sample CLBR and Prof Nick J. Pearce (Aberystwyth University) for samples FSM-3, FSM-5 and FSM-14.

References

Andersen, M. T., Jain, M., Tidemann-Lichtenberg, P., 2012. Red-IR stimulated luminescence in K-feldspar: Single or multiple trap origin? Journal of Applied Physics 112, 043507.

Bailiff, I.K., Poolton, N.R.J., 1991. Studies of charge transfer mechanisms in feldspars. Nuclear Tracks and Radiation Measurements 18, 111-118.

Bates, D.M., DebRoy, S., 2018. nls function – Nonlinear least squares. In: R Core Team and contributors worldwide, 2018. The R stats package version 3.5.0 (2018).

Baril, M.R., 2004. CCD imaging of the infra-red stimulated luminescence of feldspar. Radiation Measurements 38, 81-86.

Baril, M.R., Huntley, D.J., 2003. Optical excitation spectra of trapped electrons in irradiated feldspars. Journal of Physics: Condensed Matter 15, 8011–8027.

Bøtter-Jensen, L., Duller, G.A.T., Poolton, N.R.J., 1994. Excitation and emission spectrometry of stimulated luminescence from quartz and feldspars. Radiation Measurements 23, 613-616.

Bøtter-Jensen, L., McKeever, S.W.S., Wintle, A.G., 2003. Optically stimulated luminescence dosimetry. Elsevier, Amsterdam.

Clark, R.J., Sanderson, D.C.W., 1994. Photostimulated luminescence excitation spectroscopy of feldspars and micas. Radiation Measurements 23, 641-646.

Deer, W.A., Howie, R.A., Zussman, J., 2013. An introduction to the rock-forming minerals. Third Edition. Mineralogical Society of Great Britain and Ireland.

Duller, G.A.T., Gunn, M., Roberts, H.M., 2020. Single grain infrared photoluminescence (IRPL) measurements of feldspars for dating. Radiation Measurements 133: 106313.

Erfurt, G., 2003. Infrared luminescence of Pb^{+} centres in potassium-rich feldspars. Physica Status Solidi 200, 429-438.

607 Erfurt, G., Krbetschek, M.R., 2003. Studies on the physics of the infrared radioluminescence of
608 potassium feldspar and on the methodology of its application to sediment dating. Radiation
609 Measurements 37, 505-510.

610 Finch, A.A., Klein, J., 1999. The causes and petrological significance of cathodoluminescence
611 emissions from alkali feldspars. Contributions to Mineralogy and Petrology 135, 234-243.

612 García-Guinea, J., Correcher, V., Delgado, A., Sanchez-Muñoz, L., 2003. Cluster linkages between
613 luminescence emission spectra and continuous trap distribution in a volcanic sanidine.
614 Radiation Measurements 37, 473-477.

615 Godfrey-Smith, D.I., Cada, M., 1996. IR stimulation spectroscopy of plagioclase and potassium
616 feldspars, and quartz. Radiation Protection Dosimetry 66, 379-385.

617 Goldsmith, J.R., Laves, F., 1954. The microcline-sanidine stability relations. Geochimica et
618 Cosmochimica Acta 5, p. 1-19.

619 Hamilton, T.D.S., Munro, I.H., Walker, G., 1978. Luminescence instrumentation. In Lumb, M.D. (Ed.).
620 Luminescence spectroscopy. Academic Press, London.

621 Hütt, G., Jaek, I., Tchonka, J., 1988. Optical dating: K-feldspars optical response stimulation spectra.
622 Quaternary Science Reviews 7, 381-385.

623 Huntley, D.J., Godfrey-Smith, D.I., Thewalt, M.L.W., 1985. Optical dating of sediments. Nature 313,
624 105-107.

625 Kars, R.H., Poolton, N.R.J., Jain, M., Ankjærgaard, C., Dorenbos, P., Wallinga, J., 2013. On the trap
626 depth of the IR-sensitive trap in Na- and K-feldspar. Radiation Measurements 59, 103-113.

627 Keller, G.V., 1966. Electrical properties of rocks and minerals. Geological Society of America Memoir
628 97, 552-577.

629 Kumar, R., Kook, M., Murray, A.S., Jain, M., 2018. Towards direct measurement of electrons in
630 metastable states in K-feldspar: Do infrared-photoluminescence and radioluminescence
631 probe the same trap? Radiation Measurements 120, 7-13.

632 Kumar, R., Kook, M., Jain, M., 2020a. Understanding the metastable states in K-Na aluminosilicates
633 using novel site-selective excitation-emission spectroscopy. Journal of Physics D: Applied
634 Physics 53, 465301.

635 Kumar, R., Martin, L.I.D.J., Poelman, D., Vandenberghe, D., De Grave, J., Kook, M., Jain, M., 2020b.
636 Sie-selective mapping of metastable states using electron-beam induced luminescence
637 microscopy. Scientific Reports 10: 15650.

638 Mooney, J., Kambhampati, P., 2013. Get the basics right: Jacobian conversion of wavelength and
639 energy scales for quantitative analysis of emission spectra. Journal of Physical Chemistry
640 Letters 4, 3316-3318.

641 Poolton, N.R.J., Bøtter-Jensen, L., Johnsen, O., 1995. Influence on donor electron energies of the
642 chemical composition of K, Na and Ca aluminosilicates. Journal of Physics: Condensed
643 Matter 7, 4751-4762.

644 Poolton, N.R.J., Nicholls, J.E., Bøtter-Jensen, L., Smith, G.M., Riedi, P.C., 2001. Observation of free
645 electron cyclotron resonance in $NaAlSi_3O_8$ feldspar: Direct determination of the effective
646 electron mass. Physica Status Solidi 225, 467-475.

647 Poolton, N.R.J., Ozanyan, K.B., Wallinga, J., Murray, A.S., Bøtter-Jensen, L., 2002a. Electrons in
648 feldspar II: a consideration of the influence of conduction band-tail states on luminescence
649 processes. Physics and Chemistry of Minerals 29, 217-225.

650 Poolton, N.R.J., Wallinga, J., Murray, A.S., Bulur, E., Bøtter-Jensen, L., 2002b. Electrons in feldspar I:
651 on the wavefunction of electrons trapped at simple lattice defects. Physics and Chemistry of
652 Minerals 29, 210-216.

653 Poolton, N.R.J., Kars, R.H., Wallinga, J., Bos, A.J.J., 2009. Direct evidence for the participation of
654 band-tail states and excited state tunnelling in the luminescence of irradiated feldspars.
655 Journal of Physics: Condensed Matter 21, 485505.

656 Prasad, A.K., Poolton, N.R.J., Kook, M., Jain, M., 2017. Optical dating in a new light: A direct, non-
657 destructive probe of trapped electrons. Scientific Reports 7: 12097.

658 Riedesel, S., King, G.E., Prasad, A.K., Kumar, R., Finch, A.A., Jain, M., 2019. Optical determination of
659 the width of the band-tail states, and the excited and ground state energies of the principal
660 dosimetric trap in feldspar. Radiation Measurements 125, 40-51.

661 Riedesel, S., Bell, A.M.T., Duller, G.A.T., Finch, A.A., Jain, M., King, G.E., Pearce, N.J., Roberts, H.M.,
662 2021. Exploring sources of variation in thermoluminescence emissions and anomalous fading
663 in alkali feldspars. Radiation Measurements 141, 106541.

664 Short, M.A., 2004. Determining the possible lattice sites of two unknown defects in orthoclase from
665 the polarization effects in their optical transitions. Journal of Physics: Condensed Matter 16,
666 7405-7417.

667 Speit, B., Lehmann, G., 1982a. Radiation Defects in Feldspars. Physics and Chemistry of Minerals 8,
668 77-82.

669 Speit, B., Lehmann, G., 1982b. A comparative study of thermoluminescence and isothermal
670 destruction of radiation defects in feldspars. Journal of Luminescence 27, 127-136.

671 Stewart, D.B., Ribbe, P.H., 1969. Structural explanation for variations in cell parameters of alkali
672 feldspar with Al/Si ordering. American Journal of Science 267-A, 444-462.

673 Strickertsson, K., 1985. The thermoluminescence of potassium feldspars – glow curve characteristics
674 and initial rise measurements. Nuclear Tracks 10, 613-617.

675 Telfer, D.J., Walker, G., 1978. Ligand field bands of Mn^{2+} and Fe^{3+} luminescence centres and their site
676 occupancy in plagioclase feldspars. Modern Geology 6, 199-210.